Dimension reduction of thermo-fluid mechanisms in irradiated particle-laden turbulence

By L. Jofre, Z. R. del Rosario AND G. Iaccarino

1. Motivation and objectives

Dimensional analysis provides fundamental understanding of a physical system through the detailed examination of its units. The underlying principle of the approach is based on the notion of similarity, which postulates that relationships between physical quantities do not vary if the measurement units are changed. This central result implies that simpler small-scale experiments can be utilized to study larger-scale phenomena. In addition, one major advantage is that dimensional analysis typically yields a smaller number of independent dimensionless variables than the original measured quantities. Hence, the dimensionality of the system is reduced, and as a result fewer experiments are needed to characterize its response, i.e., quantity of interest (QoI), to a set of inputs.

1.1. *Irradiated particle-laden turbulence*

The investigation of thermal radiation interacting with particle-laden turbulent flow is of great importance in a wide range of scientific and engineering problems. For instance, phenomena reminiscent of irradiated particle-laden turbulence are ubiquitous in the fields of earth and combustion sciences, such as the impact of preferential concentration on the rate of droplet coalescence and evaporation in atmospheric clouds (Shaw, 2003; Dodd & Jofre, 2019) and the fluid mechanics of reacting boundary layers and plumes (Tieszen, 2001; Jofre & Urzay, 2017). Of particular interest to this work is the study of these physical processes in the context of volumetric particle-based receivers for energy harvesting (Ho, 2017) in concentrated solar power (CSP) systems.

Inertial particles in homogeneous isotropic turbulence (HIT) exhibit complex interactions between the phases as a result of preferential concentration and turbulence modulation (Balachandar & Eaton, 2010). Preferential concentration is the mechanism by which heavy particles tend to avoid intense vortical motions and accumulate in regions of high strain rate, whereas turbulence modulation refers to the alteration of fluid flow characteristics in the near-field region of particle clusters as a result of two-way coupling effects. The physical complexity is further increased by the simple addition of walls. In that case, turbophoresis becomes an important mechanism for augmenting the spatial inhomogeneity of the dispersed phase by driving particle accumulation at the walls.

Consequently, the analysis and characterization of particle-laden turbulent flow are challenging endeavors; many experimental and computational research studies have been devoted to this objective over the past decades, e.g., Caporaloni *et al.*, (1975); Squires & Eaton, (1991); Dunton *et al.*, (2017); Jofre *et al.*, (2019). In addition to particle-flow coupling, the problem studied in this work involves an additional layer of complexity by considering the heat transfer from the particles to the fluid via radiation absorption. The engineering application motivating the understanding of these phenomena is the improvement of energy harvesting in volumetric particle-based solar receivers. This innovative technology is expected to increase the performance of CSP plants by avoiding the

necessity of heat-exchanging stages. However, the physical mechanisms governing these systems are still not fully comprehended. Examples of recent work focusing on this problem include the interaction between radiation, particles, and buoyancy in HIT (Zamansky *et al.*, 2014), the impact of heating on the settling of particles (Frankel *et al.*, 2016), the effect of Stokes number and polydispersity on particle-gas heat transfer rates (Pouransari & Mani, 2017; Rahmani *et al.*, 2018), and the quantification of uncertainties and sensitivity analysis of complex systems (Jofre *et al.*, 2017; Masquelet *et al.*, 2017; Fairbanks *et al.*, 2020; Jofre *et al.*, 2019).

1.2. *Physical basis of dimensional analysis*

Dimensional analysis offers a general framework for reducing complex physical systems to a simpler form prior to obtaining a quantitative answer. Central to its basis is the concept of similarity (Cantwell, 2002). In physical terms, similarity refers to some equivalence between two phenomena that are quantitatively different. In mathematical form, similarity refers to a transformation that preserves some property, implying that a smaller number of variables is needed to explain the phenomenon at hand. For example, under particular conditions there is a direct relationship between the movement of large masses of air in the atmosphere and the motion of a fluid in a small-scale laboratory (or computational) model. The challenges are to find (i) those conditions and (ii) the transformation between them; in this case, the same ratio of inertial to viscous forces, i.e., Reynolds number. Dimensional analysis aims to help solve these two challenges in general problems by providing a set of mathematical techniques and methodologies.

The premise of this scientific-technical discipline is that the form of any physics-based description of a system, e.g., conservation equations and experimental correlations, must be such that the relationship between the actual physical quantities remains valid independently of the magnitudes of the base units utilized. This feature provides a number of very useful outcomes in terms of (i) facilitating the inference of similarity laws, (ii) producing a basis for out-of-scale modeling, (iii) providing support for dimensionality reduction approaches, and (iv) obtaining insight that is independent of the system of units utilized. However, it presents some limitations. For example, (i) an incomplete, or unnecessary, set of independent variables may complicate the analysis (del Rosario *et al.*, 2019), (ii) the framework is not robust to external simplifying assumptions, (iii) the set of scale-free relations obtained is not unique, and (iv) there is no formal approach to quantify the relative importance between dimensionless groups. In this regard, this work proposes a data-driven methodology aimed at addressing the last two shortfalls by means of augmenting Buckingham's π theorem with ideas developed in the fields of ridge functions (Pinkus, 2015) and active subspaces (Constantine, 2015). In addition, the physical interpretability of the results is enhanced by introducing a linear algebra approach to re-express the dimensionless groups on a user-selected basis that can be combined with inspectional analysis of the conservation equations.

1.3. *Objectives and organization of the work*

As previously introduced, the exploration and analysis of complex systems, especially multiphysics flow problems, can be systematically approached by considering the important dimensionless groups characterizing the relations between the underlying physics phenomena. Extraction of the dimensionless parameters is also very useful for engineering practice as it allows one to identify important directions in the input space for the efficient design and optimization of systems. Therefore, the objectives of this work are (i) to present a semi-empirical methodology, based on the seminal work by Constantine *et al.*,

(2017), to effectively infer important dimensionless groups from data obtained by means of computational (or laboratory) flow experiments, and (ii) to utilize the methodology to characterize important dimensionless groups in irradiated particle-laden turbulence.

Detailed descriptions of the physics modeling and computational approach utilized in this work to study irradiated particle-laden turbulence are presented by Jofre *et al.*, (2019) and Esmaily *et al.*, (2015, 2018), respectively. The remainder of the paper, therefore, is organized as follows. A detailed presentation of the data-driven dimensional analysis methodology is given in Section 2. In Section 3, the configuration of the model problem is described in terms of physics, setup, and system parameters. Next, in Section 4, results and their analysis are discussed. Finally, in Section 5, the work is concluded and future directions are proposed.

2. Data-driven dimensional analysis

In this section, we describe the integration of classical dimensional analysis with modern dimension reduction techniques. The resulting tools enable data-driven discovery of relevant dimensionless numbers, while accounting for the practical realities of large-scale simulations. The following subsections detail requisite background material.

2.1. *Dimensional analysis and the π subspace*

To enable data-driven dimensional analysis, we first connect classical techniques to a modern subspace reduction perspective. Dimensional analysis is a classical dimension reduction technique (Buckingham, 1914). Its central result is the Buckingham π theorem: Given a set of dimensional inputs $\mathbf{z} \in \mathbb{R}^{n_d}$ that predict a dimensionless QoI, i.e., $Q = f(\mathbf{z})$, the functional relationship may be re-expressed in terms of a smaller number of dimensionless numbers $\boldsymbol{\pi} \in \mathbb{R}^{n_p}$ via $\pi = \psi(\pi_1, \ldots, \pi_{n_p})$. The set of valid dimensionless inputs $\boldsymbol{\pi} = \{\pi_1, \ldots, \pi_{n_p}\}$ can be determined from the dimension matrix $\mathbf{D}$. Following the notation of del Rosario *et al.*, (2019), let $\mathbf{d}(\cdot)$ be a vectorization of the dimension function (Barenblatt, 1996). Then, the dimension matrix for $\mathbf{z}$ is given by

$$\mathbf{D} = [\mathbf{d}(\mathbf{z}_1), \ldots, \mathbf{d}(\mathbf{z}_{n_d})]. \tag{2.1}$$

Valid dimensionless numbers can be formed by products of the inputs as

$$\pi_i = \prod_{j=1}^{n_d} z_i^{v_{ij}}, \tag{2.2}$$

with the vectors $\{\mathbf{v}_j\}_{j=1}^{n_p}$ satisfying $\mathbf{D}\mathbf{v}_j = 0$. In this formulation, the Buckingham π theorem can be understood in terms of the rank-nullity theorem. In other words, the number of independent dimensionless numbers — with independence defined by the usual notion of vector independence applied to $\mathbf{v}_i$ — is given by

$$n_p = \dim(\mathcal{R}(\mathbf{D})) - \dim(\mathcal{N}(\mathbf{D})), \tag{2.3}$$

where $\dim(\cdot)$ is the subspace dimension, $\mathcal{R}(\cdot)$ denotes the range, and $\mathcal{N}(\cdot)$ denotes the nullspace. The Buckingham π theorem is silent on the choice of a basis for the nullspace of $\mathbf{D}$. The choice of appropriate dimensionless numbers is often a matter of experience. However, in this work we use data to inform a useful selection of relevant $\boldsymbol{\pi}$ groups.

To connect Buckingham's π theorem to subspace reduction, we make the following observation. Select a set of nominal conditions $\mathbf{z}_0 \in \mathbb{R}^{n_d}$ and define $x_i = \log(z_i/z_{i,0})$ for

$i = 1, \ldots, n_d$. Under this transform, we can write

$$\begin{aligned} \pi &= \psi(\exp(\mathbf{v}_1^\top \mathbf{x_1} + \log(\pi_{1,0})), \ldots, \exp(\mathbf{v}_{n_p}^\top \mathbf{x_{n_p}} + \log(\pi_{n_p,0}))), \\ &= \psi'(\mathbf{V}^\top \mathbf{x} + \log(\boldsymbol{\pi}_0)), \end{aligned} \tag{2.4}$$

where $\pi_{i,0}$ are the dimensionless numbers evaluated at the constant nominal conditions $z_{i,0}$, $\boldsymbol{\pi}_0 = [\pi_{1,0}, \ldots, \pi_{n_p,0}]^\top$, and the composition exponentiation is collapsed within ψ' to highlight mathematical structure. Intuitively, this structure exhibits variability only within a subspace of its input domain, and is invariant to orthogonal perturbations.

From Eq. (2.4), one can show that variation in the QoI occurs only through variations within $\mathcal{R}(\mathbf{V})$; since this object is derived from Buckingham's π theorem, it is called the π subspace (del Rosario *et al.*, 2019). Note that the QoI must be non-dimensionalized for this property to hold. To elucidate the importance of the π subspace, let $\mathcal{R}(\mathbf{V})^\perp$ be the orthogonal complement of $\mathcal{R}(\mathbf{V})$, and let $\mathbf{y} \in \mathcal{R}(\mathbf{V})^\perp$. Then

$$\begin{aligned} \pi(\mathbf{x} + \mathbf{y}) &= \psi'(\mathbf{V}^\top(\mathbf{x} + \mathbf{y})), \\ &= \psi'(\mathbf{V}^\top \mathbf{x} + 0), \\ &= \pi(\mathbf{x}), \end{aligned} \tag{2.5}$$

making precise the previous statement of invariance. This invariance shows that Eq. (2.4) is a ridge function in its inputs $\mathbf{x}$ (Pinkus, 2015). A restatement of this invariance is that the gradient of π is constrained. In mathematical form, note that

$$\nabla_{\mathbf{x}} \pi = \mathbf{V} \nabla_\xi \psi'(\xi), \tag{2.6}$$

and as a result the following relation is satisfied

$$\nabla_{\mathbf{x}} \pi \in \mathcal{R}(\mathbf{V}). \tag{2.7}$$

This observation will prove useful as we discuss active subspaces below. Note that while Buckingham's π theorem defines a set of valid dimensionless numbers, it does not provide a specific choice of an appropriate basis $\mathbf{V}$ (Constantine *et al.*, 2017). The function ψ' may have additional structure with further invariance properties. These properties can be expressed in terms of active subspaces.

2.2. *Active subspaces and dimensional analysis*

The active subspace is a dimension reduction concept introduced by Russi, (2010) and developed by Constantine, (2015). Let $f(\mathbf{x})$ be some differentiable QoI on a domain with integral weight $\rho(\mathbf{x}) \in \mathbb{R} \geq 0$. The active subspace is then defined in terms of the matrix

$$\mathbf{C} \equiv \int \nabla_{\mathbf{x}} f \nabla_{\mathbf{x}} f^\top \rho(\mathbf{x}) d\mathbf{x}. \tag{2.8}$$

Since $\mathbf{C}$ is by construction symmetric semi-positive definite, it admits an eigenvalue decomposition of the form $\mathbf{C} = \mathbf{U}\boldsymbol{\Lambda}\mathbf{U}^\top$. The eigenvalues need to be sorted first in decreasing order as $\lambda_1 \geq \cdots \geq \lambda_{n_d}$. Next, a threshold separating $\{\lambda_1, \ldots, \lambda_{n_d}\}$ into large $\{\lambda_1, \ldots, \lambda_{n_A}\}$ and small $\{\lambda_{n_A+1}, \ldots, \lambda_{n_d}\}$ eigenvalues is defined to generate the split $\mathbf{U} = [\mathbf{U}_A, \mathbf{U}_I]$. The final result is that the directions $\mathbf{u}_i$ are then ordered in decreasing order of importance with respect to variation in the QoI f, made quantitative by the eigenvalues. The active subspace is then given by $\mathcal{R}(\mathbf{U}_A)$, where the columns of $\mathbf{U}_A$ form a basis for the subspace.

In the case where f represents a physical equation respecting dimensional homogeneity,

Buckingham's π theorem guarantees the range constraint in Eq. (2.7). From this fact, it is clear that if $\mathbf{w} \in \mathcal{R}(\mathbf{V})^{\perp}$, we have

$$\mathbf{w}^{\top}\mathbf{C}\mathbf{w} = \mathbb{E}[\mathbf{w}^{\top}\nabla_{\mathbf{x}} f \nabla_{\mathbf{x}} f^{\top}\mathbf{w}] = 0. \tag{2.9}$$

An immediate consequence of this nullity is that if one requires the active subspace to include only those directions for which $\lambda_i > 0$, then

$$\mathcal{R}(\mathbf{U}_A) \subseteq \mathcal{R}(\mathbf{V}). \tag{2.10}$$

In words, the active subspace —computed along the transformed variables $\mathbf{x}$— is a subset of the π subspace. Furthermore, using the vector entries in Eq. (2.2), the active directions $\mathbf{u}_{A,i}$ can be directly interpreted as dimensionless groups.

The selection of the active subspace dimension n_A requires some caution. If $f(\mathbf{x}) = g(\mathbf{V}^{\top}\mathbf{x})$ is a ridge function in its inputs $\mathbf{x}$, then one can use Eq. (2.5) to show that $\lambda_i = 0$ for $i > \dim(\mathcal{R}(\mathbf{V}))$; thus, $n_A \leq \dim(\mathcal{R}(\mathbf{V}))$. However, one may also make a pragmatic choice of n_A based on preserving a user-defined level of variance in the function (Lee, 2019). We illustrate navigating these challenges in the subsections below.

2.3. *Using data-driven dimensional analysis*

Using active subspaces together with dimensional analysis enables a number of investigative approaches. The active directions can be used to produce a summary plot of the input-to-output response (Cook, 2009). A summary plot consists of a plot of the response f_i against reduced coordinates $\xi_A \equiv \mathbf{U}_A^{\top}\mathbf{x}_i$. In the case where $\dim(\mathbf{U}_A) = 1$, this can be easily visualized as a scatter plot, while $\dim(\mathbf{U}_A) = 2$ can be plotted with additional difficulty as a value-colored scatter plot.

Even when the active subspace is too high dimensional to directly visualize, the active directions $\mathbf{U}_A$ can be directly re-interpreted by re-expressing them in terms of a user-supplied basis of interpretable dimensionless numbers. Data-driven dimensional analysis identifies $\boldsymbol{\pi}$ groups which are relevant to the data at hand, but the resulting products of inputs need not involve simple powers. Conversely, the common dimensionless numbers, such as the Reynolds number, Mach number, and Prandtl number, carry physical interpretation; generally, ratios of competing effects. Re-expressing a given active direction $\mathbf{u}$ in a user-defined basis $\mathbf{V}$ of these interpretable dimensionless numbers is useful for physically interpreting the results. In practice, if one solves a linear system for weights $\mathbf{w}$ via

$$\mathbf{V}\mathbf{w} = \mathbf{u}, \tag{2.11}$$

then, the dimensionless groups represented by $\mathbf{u}$ can be re-expressed as

$$\begin{aligned} \pi &= \exp\left(\mathbf{u}_d^{\top}\mathbf{x}\right), \\ &= \exp\left(\mathbf{w}^{\top}\mathbf{V}^{\top}\mathbf{x}\right), \\ &= \exp\left(w_1(\mathbf{v}_1^{\top}\mathbf{x}) + \cdots + w_{n_p}(\mathbf{v}_{n_p}^{\top}\mathbf{x})\right), \\ &= \pi_1^{w_1} \times \cdots \times \pi_{n_p}^{w_{n_p}}. \end{aligned} \tag{2.12}$$

This allows one to construct data-driven dimensionless groups from a user-selected basis of standard dimensionless numbers, greatly aiding in physical interpretation.

2.4. *Approximating and evaluating active subspaces*

Studying active subspaces is further complicated by the realities of approximation. Generally, Eq. (2.8) cannot be computed exactly. Direct approximation of Eq. (2.8) requires

evaluation, or approximation, of the gradient $\nabla_{\mathbf{x}} f$; finite differences increase the computational complexity of simulation by a factor $d + 1$. In our target application, this corresponds to an order-of-magnitude increase.

Rather than approximating the matrix in Eq. (2.8) directly, we instead leverage recent algorithms using variable projection (Hokanson & Constantine, 2018). Conceptually, this procedure embeds a least-squares polynomial approximation within an optimization over the Grassmann manifold. The need for gradient data $\nabla_{\mathbf{x}} f$ is ameliorated by assuming a polynomial model form and target dimensionality, allowing gradient approximation based on the assumed model. In this way, one may use point evaluations $f(\mathbf{x}_i)$ in place of gradient samples $\nabla_{\mathbf{x}} f_i$, greatly reducing computational expense.

3. Description of the irradiated particle-laden turbulence system

The setup of the problem is inspired by the study of thermo-fluid mechanisms in volumetric particle-based solar receivers. The analysis of this type of system involves the interaction of particles, turbulence and radiative heat transfer. A complete description of the problem setup and system parameters is presented in the subsections below.

3.1. *Problem setup*

The study of particle-laden turbulence in an irradiated environment is performed by considering two domains. An isothermal cube of size W is utilized as a particle-laden HIT flow generator in which the fluid phase (initial density $\rho_{0,f}$ and temperature $T_{0,f}$, constant dynamic viscosity μ_f) is volumetrically forced (Bassenne *et al.*, 2016). The dispersed phase is initialized at the same time and temperature as the fluid with $N_{p,0}$ monodisperse particles (constant density ρ_p and diameter d_p) randomly distributed in the volume. The turbulence forcing scheme is targeted to produce an averaged turbulent kinetic energy, $k_{\infty,f}$, such that the ratio between domain size and Kolmogorov length scale, η, is $W/\eta \sim \mathcal{O}(10^2)$, and therefore the small-scale features of the flow are not significantly affected by the periodic boundaries. This first domain is designed to provide turbulent steady-state fluid-particle inflow conditions to the (second) radiated section.

The rectangular radiated section is of size $L \times W \times W$ in the streamwise (x, in/outflow boundaries), spanwise (y, periodic boundaries) and crossflow (z, periodic boundaries) directions, respectively. The turbulent fluid-particle flow mixture is sampled in time from a yz-plane in the HIT volume and introduced to this second domain by adding a bulk velocity U_0 to the streamwise velocity component. To achieve similar turbulence characteristics as in wall-bounded flows, the ratio between root-mean-square velocity fluctuations, u_{rms}, in the HIT domain and U_0 is selected to be $u_{rms}/U_0 \sim \mathcal{O}(10^{-1})$, and the gravitational acceleration is not considered as its effects are negligible compared to the inertia of the bulk flow. As the fluid-particle mixture flows through the domain, it is irradiated with uniform intensity I_0. The result is that particles (constant isochoric heat capacity $C_{v,p}$ and absorption coefficient ϵ_p) absorb thermal radiation, increasing their temperature, T_p, and subsequently transferring energy to the surrounding fluid (constant thermal conductivity λ_f and isobaric heat capacity $C_{P,f}$) by thermal exchange (constant fluid-particle heat convection coefficient h).

The fluid-particle mixture in this problem is optically thin, allowing us to model the radiation absorption by particles with an algebraic model; in other words, all particles receive the same amount of radiation intensity. As a result of the particles heating and transferring thermal energy to the carrier fluid, the average fluid temperature $\overline{T}_f$ in-

Parameter	Value	Parameter	Value
W	$[0.038 : 0.042]$ m	$C_{P,f}/C_{v,f}$	1.4 (diatomic ideal gases)
L	$[0.152 : 0.168]$ m	h	$[1 \cdot 10^3 : 1 \cdot 10^4]$ W/(m$^2 \cdot$ K)
T_0	$[285 : 315]$ K	$N_{p,0}$	$[9.5 \cdot 10^{5,6} : 10.5 \cdot 10^{5,6}]$
U_0	$[1 : 5]$ m/s	ρ_p	$[1 \cdot 10^3 : 1 \cdot 10^4]$ kg/m^3
$k_{\infty,f}$	$[0.1 : 0.5]$ m^2/s^2	d_p	$[1 \cdot 10^{-6} : 1 \cdot 10^{-5}]$ m
$\rho_{f,0}$	$[0.5 : 1.5]$ kg/m^3	$C_{v,p}$	$[1 \cdot 10^2 : 1 \cdot 10^3]$ J/(kg $\cdot$ K)
μ_f	$[1 \cdot 10^{-5} : 2 \cdot 10^{-5}]$ Pa $\cdot$ s	ϵ_p	$[0.25 : 0.75]$
λ_f	$[1 \cdot 10^{-2} : 3 \cdot 10^{-2}]$ W/(m $\cdot$ K)	I_0	$[9.5 \cdot 10^5 : 10.5 \cdot 10^5]$ W/m^2
$C_{P,f}$	$[1 \cdot 10^3 : 2 \cdot 10^3]$ J/(kg $\cdot$ K)		

TABLE 1. List of independent input parameters and their range of values.

creases along the streamwise direction. This deposition of energy accelerates the flow by means of thermal expansion due to a decrease in fluid density ρ_f.

3.2. *System parameters*

The study conducted in this work is designed with the objective of mimicking an experiment as it would be carried out in a laboratory facility. Following this approach, the system is characterized by 16 input parameters that can be varied independently to collect data. The list of input parameters and their range of values are described in Table 1. The ranges of W, L, T_0, and I_0 are obtained by adding 5% to/subtracting 5% from their nominal values as these are parameters that in a laboratory facility would not be easily modified in large proportions. The intervals for $\rho_{f,0}$, μ_f, λ_f, $C_{P,f}$, h, ρ_p, $C_{v,p}$, and ϵ_p are based on engineering values for material properties taken from Poling *et al.*, (2001); the generic fluid is considered to be a diatomic ideal gas resulting in $C_{P,f}/C_{v,f} = 1.4$. The levels of U_0 and $k_{\infty,f}$ are designed together to obtain realistic ratios of fluctuating-to-bulk velocity in turbulent wall-bounded flows (Pope, 2000). Finally, the ranges of d_p and $N_{p,0}$ are selected to study micron-sized particles representative of conditions in volumetric particle-based solar receivers at relatively small (case I: $N_{p,0} = 1 \cdot 10^6 \pm 5\%$) and large (case II: $N_{p,0} = 1 \cdot 10^7 \pm 5\%$) particle number densities, $n_{p,0}$.

Data are collected by computing PP-DNS of the problem for different values of the input parameters sampled from a randomized Halton sequence. A total of 256 samples have been computed for I and II (128 per case). The range of values for W, L, and $k_{\infty,f}$ are utilized to define, following the estimations described by Pope, (2000), the mesh resolution required to perform the calculations such that the significant turbulent scales are captured. The resulting Eulerian meshes for the HIT and radiated domains correspond to uniform Cartesian grids of sizes $512 \times 512 \times 512$ and $2048 \times 512 \times 512$, respectively. The time-averaging of the QoIs is computed by taking the ensemble average of 15 flow-through times (FTTs), defined as FTT $\approx L/U_0$, on yz-planes — the solution is symmetric in the y and z directions — after the first thermal transient FTT is surpassed.

4. Results and discussion

This section presents and analyzes the data acquired by computing the set of samples described in Section 3, and provides a discussion of the results obtained from the methodology introduced in Section 2.

4.1. *Data-driven inference of principal $\boldsymbol{\pi}$ groups*

Focusing on the normalized increment of fluid temperature $Q \equiv (\overline{T}_f - T_0)/T_0$, the data-driven polynomial ridge approximation strategy described in Section 2 is utilized to infer principal dimensionless groups from the data collected. This methodology requires one to approximate Q by a ridge function with a multivariate polynomial g of dimension n_p and total degree d in the form $Q \approx g(\mathbf{V}^\top \mathbf{x})$, where $\mathbf{x}$ are the log-transformed inputs. By construction, n_p imposes the number of subspace dimensions (equivalent to dimensionless groups) to be inferred, whereas d determines the degrees of freedom (polynomial order) available to fit the data along each dimension.

The adequate n_p and d values are not known *a priori*. In consequence, a study based on the coefficient of determination (CoD) is carried out to obtain suitable values for these two parameters as a first step of the methodology. The CoD, typically denoted as R^2, provides a measure of how well observed outcomes are replicated by a model relative to the proportion of total variation of outcomes explained by it. Given a dataset of $n = 128$ values $y_1, \dots y_n$, each associated with a fitted, or modeled/predicted, value $f_1, \dots f_n$ from which a residual $e_i = y_i - f_i$ can be computed, the mathematical definition of R^2 is written as

$$R^2 \equiv 1 - \frac{SS_{res}}{SS_{tot}}, \tag{4.1}$$

where $SS_{res} = \sum_{i=1}^{n}(y_i - f_i)^2 = \sum_{i=1}^{n} e_i^2$ is the residual sum of squares, and $SS_{tot} = \sum_{i=1}^{n}(y_i - \bar{y})^2$ is the total sum of squares (proportional to the variance of the data) with $\bar{y} = n^{-1}\sum_{i=1}^{n} y_i$ the mean of the observed data.

Following the statistical definition introduced above, the R^2 analysis is summarized in Figure 1 by considering Q at the outlet of I and II. The subspace dimensionality of Q slightly increases along the streamwise direction as more radiative energy is absorbed by the system. Thus, selecting n_p and d for the data at the outlet will provide a polynomial model with enough dimensions and fitting coefficients to be safely applied to infer dimensionless groups at different stations in the domain. The set of subspace dimensions and polynomial degree combinations is constrained by the amount of data available. Particularly, as shown in Figure 1, the maximum number of subspace dimensions is limited to 6, and the highest polynomial degree is restricted to 4. The cross-validation is performed by splitting the data into 8 groups of same size, and the results are represented by means of boxplots. As depicted in the figure, restricting the polynomial g to 1 dimension is not sufficient for approximating the data, especially for II, for which R^2 presents large variability skewed toward small values. In contrast, considering 3 dimensions complicates the analysis, while it does not significantly increase R^2 with respect to $n_p = 2$. Therefore, the pragmatic number of subspace dimensions for I and II is 2, constructed by utilizing polynomial degrees equal to 3 and 4, respectively. This selection results in R^2 values presenting small variability and close to 1.

As introduced in Section 2, the projection weights $\mathbf{v}_1$ and $\mathbf{v}_2$ correspond, respectively, to the exponents of the input parameters composing each of the two principal dimensionless groups, π_1 and π_2, approximated by the polynomial ridge function. The labeling of these two groups has been arranged such that π_1 is the subspace most aligned with the

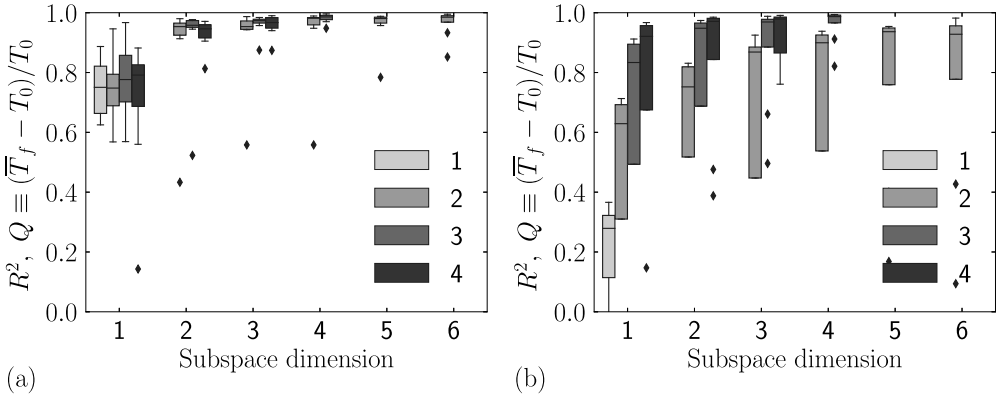

FIGURE 1. Coefficient of determination, R^2, results of different subspace dimension and post-projection polynomial-fit order models for $Q \equiv (\overline{T}_f - T_0)/T_0$ at the outlet for I (a) and II (b). The grayscale color scheme indicates the polynomial order of the model.

principal direction obtained from approximating the data with a one-dimensional polynomial ridge function. The $\mathbf{V}$ values are very similar for I and II. This result indicates that the two cases investigated exhibit equivalent behavior in terms of important dimensionless groups, and consequently the analysis below discusses them together by considering I. The R^2 results depicted in Figure 1 show that the first subspace dimension accounts for almost 80% of the variation in the data. Focusing on the first subspace dimension, the data-driven inferred expression for the dimensionless group π_1 for $Q \equiv (\overline{T}_f - T_0)/T_0$ at the outlet of the radiated section is given by

$$\pi_1 = W^{-0.510} \times L^{0.612} \times T_0^{-0.414} \times U_0^{-0.174} \times k_{\infty,f}^{-0.002} \times \rho_{f,0}^{-0.104} \times \mu_f^{0.001} \times \lambda_f^{-0.010} \times C_{P,f}^{-0.161} \times h^{0.013} \times N_{p,0}^{0.045} \times \rho_p^{-0.146} \times d_p^{0.002} \times C_{v,p}^{-0.095} \times \epsilon_p^{0.210} \times I_0^{0.224}. \quad (4.2)$$

Analogously, the inferred definition for π_2 is

$$\pi_2 = W^{-0.084} \times L^{-0.491} \times T_0^{-0.422} \times U_0^{-0.069} \times k_{\infty,f}^{0.027} \times \rho_{f,0}^{-0.097} \times \mu_f^{-0.074} \times \lambda_f^{0.053} \times C_{P,f}^{-0.076} \times h^{0.007} \times N_{p,0}^{0.478} \times \rho_p^{0.113} \times d_p^{0.535} \times C_{v,p}^{-0.032} \times \epsilon_p^{0.084} \times I_0^{0.101}. \quad (4.3)$$

These expressions provide a quantitative decomposition of the principal $\boldsymbol{\pi}$ groups as a function of the independent (input) parameters of the problem. A more insightful, and easier to interpret, decomposition in terms of standard fluid mechanics dimensionless numbers is discussed in the next subsection.

The input-to-output response of Q at the outlet of the radiated domain as a function of the $\boldsymbol{\pi}$ groups inferred by the ridge function polynomial is depicted in Figure 2. The fit obtained by the first subspace dimension shown in Figure 2(a) reveals that Q increases monotonically with π_1, and presents exponential growth for $\pi_1 > 1$. In addition, the two-dimensional summary plot depicted in Figure 2(b) qualitatively indicates that Q generally increases also with π_2. However, as shown by the plot, the importance of this second dimensionless group is significantly small with respect to π_1 as most of the variation in the data (grayscale color gradient) is captured by the latter.

4.2. *Interpretation in terms of standard dimensionless numbers*

The data-driven methodology described in Section 2 allows one to easily re-express the $\boldsymbol{\pi}$ groups as powers of standard dimensionless numbers, Eq. (2.12), through the simple

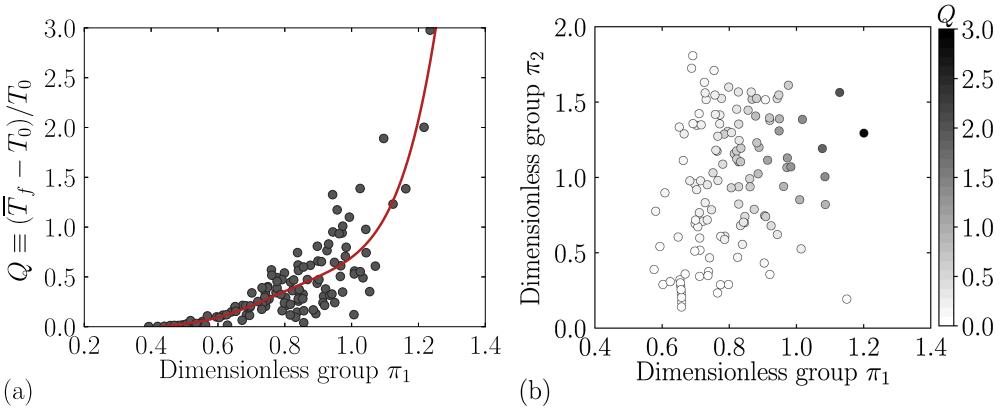

FIGURE 2. Summary plots of the 2-D ridge function fit versus the inferred dimensionless groups π_1 (a) and (b) $\pi_1 - \pi_2$ with a 3$^{\text{rd}}$ degree polynomial for $Q \equiv (\overline{T}_f - T_0)/T_0$ of I at the outlet.

linear algebra transformation given in Eq. (2.11). As a basis for re-expression of the $\boldsymbol{\pi}$ groups, we consider widely recognized dimensionless numbers in fluid mechanics resulting from normalizing the equations and boundary conditions describing the problem (Jofre *et al.*, 2019). Their definitions are given in Table 2, where the relaxation time of the flow based on the Kolmogorov scale is $\tau_\eta = \lambda_T/(\sqrt{15}u_{rms})$ and its associated length scale corresponds to $\eta = u_{rms}\tau_\eta$. In addition, particles are assumed to be perfectly spherical with mass $m_p = \pi\rho_p d_p^3/6$.

Utilizing the set of dimensionless numbers listed in Table 2 as the transformation basis, the π_1 and π_2 dimensionless groups inferred from data in the previous subsection can be re-expressed as products of standard fluid mechanics groups. The decomposition for the first dimensionless group corresponds to

$$\begin{aligned}\pi_1 = {} & AR^{0.591} \times {N_{p,0}}^{0.062} \times Ma^{0.146} \times Pr^{0.036} \times Nu^{0.004} \times \chi^{0.154} \\ & \times {Re_\lambda}^{-0.297} \times MLR^{-0.017} \times {St_\eta}^{0.153} \times {Re_W}^{0.120} \times {\epsilon_p}^{0.210} \times \mathcal{R}^{0.278}, \end{aligned} \tag{4.4}$$

$$\approx \frac{AR^{0.6} \times {\epsilon_p}^{0.2} \times \mathcal{R}^{0.3}}{{Re_\lambda}^{0.3}}, \tag{4.5}$$

and for the second group is given by

$$\begin{aligned}\pi_2 = {} & AR^{-0.464} \times {N_{p,0}}^{0.167} \times Ma^{0.189} \times Pr^{0.050} \times Nu^{-0.062} \times \chi^{0.074} \\ & \times {Re_\lambda}^{-0.621} \times MLR^{0.311} \times {St_\eta}^{-0.071} \times {Re_W}^{0.136} \times {\epsilon_p}^{0.084} \times \mathcal{R}^{0.169}, \end{aligned} \tag{4.6}$$

$$\approx \frac{MLR^{0.3}}{AR^{0.5}{Re_\lambda}^{0.6}}, \tag{4.7}$$

where a threshold of $|w_{ij}| \geq 0.2$ has been utilized to obtain the approximated $\boldsymbol{\pi}$ groups.

The structure of the two dimensionless groups rounded in Eqs. (4.5) and (4.7) indicates that AR and Re_λ play a major role in dictating the system's response in terms of $Q \equiv (\overline{T}_f - T_0)/T_0$ as they contribute to both π_1 and π_2. The first dimensionless group, π_1, also involves the radiometric dimensionless numbers ϵ_p and $\mathcal{R}$, and consequently is largely connected to the transfer of radiative energy encompassing the absorption by particles and the subsequent deposition to the carrier phase as the mixture is advected through the radiated domain. Instead, π_2 includes MLR, and therefore is related to the number of particles with respect to the fluid phase. For example, the composition of π_1 indicates

Dimensionless number	Definition
Kinematic groups:	
Domain aspect ratio	$AR = L/W$
Number of particles	$N_{p,0} = n_{p,0}\lambda_T^3$
Thermophysical groups:	
Mach number	$Ma = u_{rms}/\sqrt{\gamma R_f T_0}$
Prandtl number	$Pr = C_{P,f}\mu_f/\lambda_f$
Adiabatic index	$\gamma = C_{P,f}/C_{v,f}$
Nusselt number	$Nu = hd_p/\lambda_f$
Particle-fluid heat capacities	$\chi = C_{v,p}/C_{v,f}$
Hydrodynamic groups:	
Taylor Reynolds number	$Re_\lambda = \rho_{f,0}u_{rms}\lambda_T/\mu_f$
Mass loading ratio	$MLR = n_{p,0}m_p/\rho_{f,0}$
Kolmogorov Stokes number	$St_\eta = \tau_p/\tau_\eta$
Bulk Reynolds number	$Re_W = \rho_{f,0}U_0W/\mu_f$
Radiometric groups:	
Particles absorption coefficient	ϵ_p
Radiation transfer number	$\mathcal{R} = \lambda_T\pi d_p^2 I_0/(4T_0U_0m_pC_{v,p})$

TABLE 2. List of standard fluid mechanics dimensionless numbers. The adiabatic index is assumed constant in this work (diatomic ideal gases: $\gamma = 1.4$), and therefore is not considered an independent dimensionless number. The radiation transfer number $\mathcal{R}$ is similar to the Damköhler number in chemically reacting flows.

that augmenting AR, ϵ_p, and/or $\mathcal{R}$ results in an increase of Q, while enlarging Re_λ translates into decreasing Q.

Focusing on π_1, which accounts for most of the variation in Q, the larger the length L of the radiated domain with respect to W, the more energy is absorbed by the system, resulting in higher fluid temperatures at the outlet. However, AR may be imposed, or constrained, in practical engineering problems. In that case, ϵ_p, $\mathcal{R}$, and Re_λ become the most sensitive parameters for controlling the thermal response of irradiated particle-laden turbulence systems.

5. Conclusions

Multiphysics flow problems, such as irradiated particle-laden turbulence, involve the analysis (typically) of complex high-dimensional parameter spaces. Their study can be systematically approached by considering important dimensionless groups characterizing the underlying physics phenomena, which, in addition to reducing the dimensionality of the system, provide excellent support for the inference of similarity laws and a basis for out-of-scale modeling. However, classical dimensional analysis techniques present two main shortfalls as the set of scale-free groups are not unique, and there is no general methodology for quantifying their relative importance and physically interpreting the results. This work, therefore, has proposed a data-driven methodology aimed to address these deficiencies by augmenting Buckingham's π theorem with ideas developed in the

fields of ridge functions and active subspaces tailored to the study of large-scale, complex turbulent flow applications.

The data-driven methodology presented has been utilized to infer important dimensionless groups of the problem. Two dimensionless groups have been identified by approximating the active subspaces of the data with polynomial ridge functions. Their decomposition in terms of standard fluid mechanics dimensionless numbers indicate that the mass loading ratio MLR and especially the aspect ratio AR, the Taylor Reynolds number Re_λ, the particle absorption coefficient ϵ_p, and the radiation transfer number $\mathcal{R}$ contribute the most to the variation of the system's thermal response in terms of fluid temperature at the outlet of the radiated domain. The CoD achieved by considering the first dimensionless group is approximately 80%, and increases to practically 100% when considering the two groups together. Its analysis, combined with the scale-free conservation equations, shows that, rather than the distribution of particles and thermophysical properties of the two (carrier and dispersed) phases, the absorption of radiation by particles, the radiative energy deposition rate, and the turbulent flow mixing are the most important mechanisms for controlling the temperature of the fluid in the system. The results are similar for the two cases considered, which differ by an order of magnitude in the number of particles, and therefore suggest that they may be generalizable to wider ranges of dispersed phase loading.

Future work will focus on expanding the data-driven methodology to generate simplified decompositions of the dimensionless groups inferred by means of L1-regularization (Lasso regression) approaches. In addition, wider ranges of dispersed phase loading will be analyzed to further corroborate the scientific findings described in this work, and to carry out studies for the engineering optimization of radiative energy transfer in particle-laden turbulent flows.

Acknowledgments

This investigation was funded by the Advanced Simulation and Computing (ASC) program of the US Department of Energy's National Nuclear Security Administration via the PSAAP-II Center at Stanford, Grant No. DE-NA0002373.

REFERENCES

Balachandar, S. & Eaton, J. K. 2010 Turbulent dispersed multiphase flow. *Annu. Rev. Fluid Mech.* **42**, 111–133.

Barenblatt, G. I. 1996 *Scaling, Self-Similarity, and Intermediate Asymptotics: Dimensional Analysis and Intermediate Asymptotics*. Cambridge University Press.

Bassenne, M., Urzay, J., Park, G. I. & Moin, P. 2016 Constant-energetics physical-space forcing methods for improved convergence to homogeneous-isotropic turbulence with applications to particle-laden flows. *Phys. Fluids* **28**, 035114.

Buckingham, E. 1914 On physically similar systems; illustrations of the use of dimensional equations. *Phys. Rev.* **4**, 345–376.

Cantwell, B. J. 2002 *Introduction to Symmetry Analysis*. Cambridge University Press.

Caporaloni, M., Tampieri, F., Trombetti, F. & Vittori, O. 1975 Transfer of particles in nonisotropic air turbulence. *J. Atmos. Sci.* **32**, 565–568.

Constantine, P. G. 2015 *Active Subspaces: Emerging Ideas for Dimension Reduction in Parameter Studies*. SIAM Philadelphia.

Constantine, P. G., del Rosario, Z. & Iaccarino, G. 2017 Data-driven dimensional analysis: algorithms for unique and relevant dimensionless groups. *arXiv:1708.04303*.

Cook, R. D. 2009 *Regression Graphics: Ideas for Studying Regressions Through Graphics*. John Wiley & Sons.

Dodd, M. S. & Jofre, L. 2019 Small-scale flow topologies in decaying isotropic turbulence laden with finite-size droplets. *Phys. Rev. Fluids* **4**, 064303.

Dunton, A. M., Jofre, L., Doostan, A. & Iaccarino, G. 2017 Pass-efficient methods for compression of high-dimensional turbulent flow data. *Annual Research Briefs*, Center for Turbulence Research, Stanford University, pp. 313–325.

Esmaily, M., Jofre, L., Iaccarino, G. & Mani, A. 2015 A scalable geometric multigrid method for non-symmetric linear systems arising from elliptic equations. *Annual Research Briefs*, Center for Turbulence Research, Stanford University, pp. 211–223.

Esmaily, M., Jofre, L., Mani, A. & Iaccarino, G. 2018 A scalable geometric multigrid solver for nonsymmetric elliptic systems with application to variable-density flows. *J. Comput. Phys.* **357**, 142–158.

Fairbanks, H. R., Jofre, L., Geraci, G., Iaccarino, G. & Doostan, A. 2020 Bi-fidelity approximation for uncertainty quantification and sensitivity analysis of irradiated particle-laden turbulence. *J. Comput. Phys.* **402**, 108996.

Frankel, A., Pouransari, H., Coletti, F. & Mani, A. 2016 Settling of heated particles in homogeneous turbulence. *J. Fluid Mech.* **792**, 869–893.

Ho, C. K. 2017 Advances in central receivers for concentrating solar applications. *Sol. Energy* **152**, 38–56.

Hokanson, J. M. & Constantine, P. G. 2018 Data-driven polynomial ridge approximation using variable projection. *SIAM J. Sci. Comput.* **40**, A1566–A1589.

Jofre, L. & Urzay, J. 2017 Interface dynamics in the transcritical flow of liquid fuels into high-pressure combustors. *AIAA Paper* 2017-4040.

Jofre, L., Geraci, G., Fairbanks, H. R., Doostan, A. & Iaccarino, G. 2017 Multi-fidelity uncertainty quantification of irradiated particle-laden turbulence. *Annual Research Briefs*, Center for Turbulence Research, Stanford University, pp. 21–34.

Jofre, L., Domino, S. P., & Iaccarino, G. 2019 Eigensensitivity analysis of subgrid-scale stresses in large-eddy simulation of a turbulent axisymmetric jet. *Int. J. Heat Fluid Fl.* **77**, 314–335.

Jofre, L., Papadakis, M., Roy, P. T., Aiken, A. & Iaccarino, G. 2019 Multifidelity modeling of irradiated particle-laden turbulence subject to uncertainty. *Int. J. Uncertain. Quan.* Submitted.

Lee, M. R. 2019 Modified active subspaces using the average of gradients. *SIAM-ASA J. Uncertain. Quan.* **7**, 53–66.

Masquelet, M., Yan, J., Dord, A., Laskowski, G., Shunn, L., Jofre, L. & Iaccarino, G. 2017 Uncertainty quantification in large eddy simulations of a rich-dome aviation gas turbine. In *Proc. ASME Turbo Expo 2017, #GT2017-64835*.

Pinkus, A. 2015 *Ridge Functions*. Cambridge University Press.

Poling, B. E., Prausnitz, J. M. & O'Connell, J. P. 2001 *The Properties of Gases and Liquids*. McGraw-Hill.

Pope, S. B. 2000 *Turbulent Flows*. Cambridge University Press.

Pouransari, H. & Mani, A. 2017 Effects of preferential concentration on heat transfer in particle-based solar receivers. *J. Sol. Energy Eng.* **139**, 021008.

Rahmani, M., Geraci, G., Iaccarino, G. & Mani, A. 2018 Effects of particle polydispersity on radiative heat transfer in particle-laden turbulent flows. *Int. J. Multiphas. Flow* **104**, 42–59.

del Rosario, Z., Lee, M. & Iaccarino, G. 2019 Lurking variable detection via dimensional analysis. *SIAM-ASA J. Uncertain. Quan.* **7**, 232–259.

Russi, T. M. 2010 Uncertainty quantification with experimental data and complex system models. PhD thesis, UC Berkeley.

Shaw, R. A. 2003 Particle-turbulence interactions in atmospheric clouds. *Annu. Rev. Fluid Mech.* **35**, 183–227.

Squires, K. D. & Eaton, J. K. 1991 Preferential concentration of particles by turbulence. *Phys. Fluids A* **3**, 1169–1178.

Tieszen, S. R. 2001 On the fluid mechanics of fires. *Annu. Rev. Fluid Mech.* **33**, 67–92.

Zamansky, R., Coletti, F., Massot, M. & Mani, A. 2014 Radiation induces turbulence in particle-laden fluids. *Phys. Fluids* **26**, 071701.